Journal of Power Sources 580 (2023) 233272

Contents lists available at ScienceDirect

Journal of Power Sources

journal homepage: www.elsevier.com/locate/jpowsour

Efficient computation of safe, fast charging protocols for multiphase lithium-ion batteries: A lithium iron phosphate case study

Giacomo Galuppini, Marc D. Berliner, Huada Lian, Debbie Zhuang, Martin Z. Bazant, Richard D. Braatz *

Massachusetts Institute of Technology, Cambridge, MA 02139, USA

HIGHLIGHTS

- Fast charging protocols designed for multiphase batteries.
- Computationally efficient protocol design by solving as a hybrid simulation.
- Protocols designed for commercial lithium-ion batteries.
- Protocols minimize charging time, subject to safety and operational constraints.
- First such analysis based on Multiphase Porous Electrode Theory.

ARTICLE INFO

Keywords:
Lithium-ion batteries
Lithium iron phosphate
Multiphase Porous Electrode Theory
Fast charging
Charging protocols
Optimal control

ABSTRACT

Fast charging is a desirable feature for lithium-ion batteries. Charging at high currents, however, can damage the battery and accelerate aging processes. Fast charging protocols are typically computed by solving an optimization in which the cost function and constraints encode the conflicting requirements of safety and speed. A key element of the optimization is the choice of the dynamic model of the battery, with an inherent tradeoff between model accuracy and computational complexity. An oversimplified model may result in unreliable protocols, whereas a complex model may result in an optimization that is too computationally expensive to be suitable for real-time applications. This article describes an approach for embedding a complex battery model into charging optimization while having low computational cost. Multiphase Porous Electrode Theory is used to provide an accurate description of batteries characterized by multiphase materials, and the optimization is solved by transformation into mixed discrete-continuous simulation of a set of Differential–Algebraic Equations. The methodology is applied to an MPET model of commercially available Lithium Iron Phosphate batteries. Protocols based on a variety of operational constraints are computed to assess both the effectiveness of the approach, and the advantages and disadvantages of the charging protocols.

1. Introduction

Lithium-ion batteries are the leading technology for energy storage, for a huge range of devices (e.g., laptops, cell phones, automobiles), as well as for smart grid applications [1,2]. Further spread of this technology, however, is still limited by the time required for charging operations. This problem is particularly significant for electric vehicles, where long charging times represent one of the main worries for the vehicle end-user [3]. The design of suitable fast charging protocols for lithium-ion batteries is however complicated by the inherent tradeoffs between charging at high C-rates and preserving safety of operations and battery lifetime [4,5]. Specifically, operating the battery at high C-rates accelerates its aging due to higher temperatures, increased growth rate of the solid-electrolyte interface (SEI) layer, increased lithium plating, and higher mechanical stresses [6–12]. The development of advanced battery management systems (ABMS) that provide safe, fast, and reliable charging is therefore receiving a lot of attention from the research community [13–16]. In particular, fast charging protocols have been designed by dynamic optimization [17,18], Model Predictive Control (MPC) [19–22], and Bayesian Optimization (BO) approaches [23,24]. The design problem is formulated as constrained optimization, with the aim of minimizing the charging time while fulfilling constraints encoding the battery dynamics, as well as safety of operations and reduced lifetime degradation.

Detailed models of the dynamic behavior of lithium-ion batteries consist of a (possibly huge) set of Differential–Algebraic Equations

* Corresponding author.
E-mail address: braatz@mit.edu (R.D. Braatz).

https://doi.org/10.1016/j.jpowsour.2023.233272
Received 11 March 2023; Received in revised form 6 May 2023; Accepted 29 May 2023
Available online 15 June 2023

(DAEs) [25–28]. The solution of optimizations involving DAEs can require very high computational cost and/or computational time [25,27]. For these reasons, online studies often use reformulated or reduced-order models, which provide computational efficiency at the cost of great simplifications the physics captured by the model [29–33].

An inaccurate description of the battery dynamics may, however, result in unreliable charging protocols, or in misleading interpretations of actual performance. This issue is even more prevalent for batteries with active materials that have multiple stable phases, whose dynamics include hysteresis, oscillations, and non-monotonic evolution of battery states. For multiphase materials, a modeling approach is required to correctly capture the dynamics of such systems, since conventional Porous Electrode Theory (PET), typically exploited for detailed battery simulations, does not allow for a description of such phenomena [34]. The computational complexity of multiphase-specific models are, however, much higher than that of standard PET. This high model complexity calls for the development of an efficient approach for the computation of charging protocols.

With these premises, the aim of this work is to propose an efficient approach for the computation of safe, fast charging protocols for batteries built with multiphase materials. This approach combines Multiphase Porous Electrode Theory (MPET) [34–36] with the concept of general battery operating mode [37,38]. MPET exploits nonequilibrium thermodynamics to model phase-separating materials, for which the voltage is an emergent property of inhomogeneous concentration profiles, even in equilibrium [34–36]. The interpretation of a charging protocol as a sequence of battery operating modes allows approaching the charging protocol design by running a mixed discrete-continuous simulation, instead of solving a dynamic optimization [37]. An operating mode (such as constant current, voltage, or temperature) can be simulated by appending a single algebraic equation to the set of DAEs defining the battery model. In this way, the computational complexity of the dynamic optimization is drastically reduced, and a detailed MPET model of the batteries can be leveraged even for online computations.

The approach for design of safe, fast charging protocols is developed in this work with a freely available implementation of MPET, and a model of A123 System's *APR18650M1A* Lithium Iron Phosphate (LFP) batteries [39]. The effectiveness of the approach is demonstrated for scenarios involving constraints on power, lithium-plating overpotential, temperature, and/or electrolyte and solid-phase concentrations. This work is the first to use MPET in the computation of optimal charging protocols, and the first to apply the general operating mode approach [37,38] to the design of fast charging protocols for LFP batteries (past literature on fast charging LFP batteries has been primarily on linear or multistage design [6,7,17,23,40], or pulsed design [40]).

The article is organized as follows: Section 2.1 summarizes MPET and compares to PET; Section 2.2 discusses the MPET implementation as a set of DAEs; Section 2.3 describes the concept of general battery operating modes and discusses the implementation of the operating modes exploited in this work; and Section 2.4 discusses the methodology for the computation of safe, fast charging protocols via simulation. A suite of protocols are computed and analyzed in Section 3, whereas Section 4 provides further discussion of the design methodology. Finally, Section 5 summarizes the main findings of this work.

2. Materials and methods

This section describes the methodology used in this article for the computation of safe, fast charging protocols for multiphase lithium-ion batteries. To this end, the MPET modeling approach is introduced and compared to standard PET to highlight their differences. Then some basic definitions of DAEs are given, and the concept of general operating modes battery is discussed, with several examples. Finally, the overall algorithm for the computation of charging protocols is presented and discussed.

2.1. Multiphase porous electrode theory

Lithium-ion batteries are typically built using two porous electrodes and a porous separator between them. A porous electrode is defined as a composite solid containing interconnected void space that constitutes a significant portion of the volume. These void spaces are filled by the liquid electrolyte [41]. During charge, the lithium ions contained in the active material of the positive electrode migrate towards the active material of the negative electrode, and undergo several transport and electrochemical reaction processes. PET [42] represents a well-established approach to model this complex dynamic behavior. The transport of lithium ions between active particles in the electrolyte is described by Stefan–Maxwell concentrated solution theory, while the two main phases in each electrode (solid active material and electrolyte) are coupled by Butler–Volmer (BV) kinetics. Finally, solid-phase transport is modeled as Fickian diffusion. Typically, PET models are implemented with a *pseudo-two-dimensional* (P2D) approach, where the principal dimension is the position between the two metal contact points on the opposite sides of the battery, while the second, "pseudo" dimension is the distance from the center of a solid particle.

PET has been developed and tested for a variety of battery materials (e.g., lithium nickel cobalt, nickel manganese cobalt), and a number of software implementations are available [25–28,43–46], based on free (e.g., [25,28]) and commercial modeling languages (e.g., [27,46]). Standard PET models rely on *empirical* models of the thermodynamics of the active materials, typically obtained by fitting one or more Open Circuit Voltage (OCV) versus State Of Charge (SOC) measurements. Active materials with thermodynamics resulting in multiple stable phases (e.g., lithium iron phosphate and graphite) are not described by PET, except by certain empirical modifications, which unavoidably mask the true thermodynamic behavior. MPET [34,35] was developed which properly describes the thermodynamics of multiphase materials. MPET handles multiphase materials by modeling the free energy functional, rather than the voltage directly, and consistently defining electrochemical activities, overpotentials, and reaction rates. MPET describes the solid-state dynamics by relying on multiple, interacting particles, placed both along the length of the electrode and in parallel with each other in terms of electrolyte access. Each particle is characterized by size and conductance values, which in turn are drawn from suitable lognormal distributions. Moreover, several particle shapes (spheres, cylinders, or rectangular approximation of platelet particles, reacting on the b plane only) and active particle models, e.g., homogeneous, Allen–Cahn Reaction (ACR) or Cahn–Hilliard Reaction (CHR), can be considered for particles in the two electrodes [34], which extend the original Allen–Cahn [47] and Cahn–Hilliard [48] models, respectively, for electrochemical reactions [49]. MPET also provides alternatives to the empirical BV model of reaction kinetics typically adopted in PET, based on Marcus theory of electron transfer [50–52] and its generalization for lithium intercalation by coupled ion-electron transfer [53]. Finally, the electrolyte can be specified either as a dilute model or using a full Stefan–Maxwell concentrated solution theory [34]. This enhanced modeling of multiphase materials has been validated by many experiments, including direct imaging of non-equilibrium phase separation in single particles [49,54–58] and porous electrodes [36,59–61].

Negative lithium-plating overpotential values typically trigger side reactions which eventually degrade the battery lifetime. Recently, lithium plating was found to initiate well below 0.0 V vs. Li^+/Li due to the nucleation barrier of forming lithium metal on the substrates [56,61–63]. To study the impact of fast charging on lithium-plating, a nucleation barrier is incorporated into the lithium-plating reaction, and the phase-field model for graphite is applied to resolve the competition of lithium intercalation and plating reaction in a porous graphite anode. Furthermore, to analyze how fast charging could affect the cell temperature, a nonisothermal model is incorporated [27,64]. Electrolyte heat transport modeling is implemented exactly as in [64]. Heat generation is generated from a sum of reversible heat generation from the

electrochemical reaction at the particle scale rescaled to the electrode scale, Ohmic heat generation, and diffusive heat transport from the electrolyte and solid porous material as in [27]. Only heat generation from overpotential and not from entropy is included in this model, as different reformulations of the derivation of nonisothermal heat generation terms are included in MPET as in the Newman derivation of nonisothermal heat generation [27,65].

The simulations performed in this article are based on the freely available Python implementation of MPET [34], which is further enhanced to include lithium plating and nonisothermal modeling, as described above.

2.2. Differential–algebraic equations

Both the PET and MPET models can be formulated as a system of DAEs. This numerical modeling approach allows the inclusion of all the governing laws required by the model in a single set of differential and algebraic equations. DAEs can be specified in the general *fully implicit* form:

$$F(t, \dot{y}(t), y(t)) = 0 \tag{1}$$

where t is time, $y(t)$ is the vector of states, $\dot{y}(t)$ is its time derivative, and F is the vector of residuals. Alternatively, DAEs can be specified in *mass matrix* form:

$$M(t)\dot{y}(t) = f(t, y(t)) \tag{2}$$

where M is the square mass matrix and f is the residual. The differential states of an MPET model include electrolyte concentration c_e (i.e., concentration of lithium in the electrolyte), solid particle concentrations c_s (i.e., concentration of lithium in the active material particles), and temperature T, whereas algebraic states include ionic fluxes j, electrolyte potential Φ_e, and solid particle potentials Φ_s.

At each time instant $\bar{t}$, the DAE solver computes both the time derivative of differential terms $\dot{y}(\bar{t})$, and the value of algebraic terms $y(\bar{t})$ [66,67]. Specifically, the MPET implementation in [34] is based on the Python package *DAE Tools* [68], which enables a high-level handling of DAEs, as well as hybrid modeling by means of logic conditions and State Transition Networks (STNs) [69]. In turn, DAE Tools leverages the *SUNDIALS* suite [66] as a low-level DAE solver.

2.3. Battery general operating modes

Standard PET and MPET implementations typically offer constant current, voltage, and power operation modes [25,27,28], where the user can specify a value for current, voltage, or power. This concept can be generalized to consider arbitrary states involved in the battery dynamics [37]. In a generic operating mode, the desired time behavior of the state of interest (e.g., voltage, power, temperature, etc.) can be enforced by including current among the states of the DAE system, and appending a specific constraint involving the state of interest. Then the solution of this augmented set of DAEs allows computing the time evolution of the current resulting in the desired time evolution of the variable of interest.

Consider a generic *algebraic* variable of interest ξ, and the corresponding operating mode of constant ξ. Let $\overline{\xi}$ be the desired constant value for ξ. The current, $I(t, \dot{y}(t), y(t))$, is then treated as a state of the DAE system, and its time evolution defined by the residual:

$$I(t, \dot{y}(t), y(t)) : \quad \xi(t, \dot{y}(t), y(t)) - \overline{\xi} = 0. \tag{3}$$

A function $I(t, \dot{y}(t), y(t))$ satisfying (3), together with the DAEs defining the battery model, gives a current evolution resulting in the desired value of ξ. This approach can be straightforwardly extended to require arbitrary evolutions of ξ. This extension is achieved by defining a desired functional form $\overline{\xi}(t, \dot{y}(t), y(t))$ to be used in place of $\overline{\xi}$ in (3):

$$I(t, \dot{y}(t), y(t)) : \quad \xi(t, \dot{y}(t), y(t)) - \overline{\xi}(t, \dot{y}(t), y(t)) = 0. \tag{4}$$

This approach does not require that $I(t, \dot{y}(t), y(t))$ can be solved for algebraically, thus allowing for arbitrary, nonlinear relations between $I(t, \dot{y}(t), y(t))$ and $\overline{\xi}(t, \dot{y}(t), y(t))$.

Instead, if the variable of interest ξ is a *differential* variable, its evolution cannot be directly forced. Instead, its time derivative $\overline{\frac{d\xi}{dt}}(t, \dot{y}(t), y(t))$ can be forced by including the constraint

$$I(t, \dot{y}(t), y(t)) : \quad \frac{d\xi}{dt}(t, \dot{y}(t), y(t)) - \overline{\frac{d\xi}{dt}}(t, \dot{y}(t), y(t)) = 0 \tag{5}$$

in the set of DAEs.

The reminder of this section defines the battery operating modes analyzed in this work.

2.3.1. Constant Current (CC) mode

Let $\overline{I}$ be the value of the constant current in CC mode. The current $I(t, \dot{y}(t), y(t))$ is an algebraic state of the DAEs, and its time evolution is defined by the residual

$$I(t, \dot{y}(t), y(t)) : \quad I(t, \dot{y}(t), y(t)) - \overline{I} = 0. \tag{6}$$

2.3.2. Constant Voltage (CV) mode

Let $\overline{V}$ be the desired value of the constant voltage in CV mode. The cell voltage $V(t, \dot{y}(t), y(t))$ is an algebraic state defined by

$$V(t, \dot{y}(t), y(t)) = \Phi_s(v, t, \dot{y}(t), y(t))|_{v=1} - \Phi_s(v, t, \dot{y}(t), y(t))|_{v=V_{tot}} \tag{7}$$

where Φ_s is the solid potential and v is the index of the vth discrete volume along the principal dimension of the battery ($v = 1$ corresponding to the volume at cathode/current collector interface, and $v = V_{tot}$ corresponding to the volume at the anode/current collector interface). The current time evolution resulting in the desired voltage can be obtained with the constraint

$$I(t, \dot{y}(t), y(t)) : \quad V(t, \dot{y}(t), y(t)) - \overline{V} = 0. \tag{8}$$

2.3.3. Constant Power (CP) mode

Let $\overline{P}$ be the value of the desired constant power in CP mode. The cell power $P(t, \dot{y}(t), y(t))$ is an algebraic state, defined by

$$P(t, \dot{y}(t), y(t)) = V(t, \dot{y}(t), y(t)) \times I(t, \dot{y}(t), y(t)). \tag{9}$$

The current time evolution resulting in the desired power can be obtained with the constraint

$$I(t, \dot{y}(t), y(t)) : \quad P(t, \dot{y}(t), y(t)) - \overline{P} = 0. \tag{10}$$

2.3.4. Constant Lithium-plating Overpotential (CLO) mode

Let $\overline{\eta}_p$ be the desired constant value of the local lithium-plating overpotential. The lithium-plating overpotential $\eta_p(v, p, t, \dot{y}(t), y(t))$ is an algebraic state defined by

$$\eta_p(v, p, t, \dot{y}(t), y(t)) = \Phi_s(v, p, t, \dot{y}(t), y(t)) - \Phi_e(v, t, \dot{y}(t), y(t)) + \Phi_n \tag{11}$$

where Φ_s is the particle solid potential, Φ_e is the electrolyte potential, Φ_n is the nucleation barrier, v is the index of the vth discrete volume along the principal dimension of the battery, and p is the index of the pth particle within the considered volume. The current time evolution resulting in the desired lithium-plating overpotential for the pth particle of the vth volume can be obtained with the constraint

$$I(t, \dot{y}(t), y(t)) : \quad \eta_p(v, p, t, \dot{y}(t), y(t)) - \overline{\eta}_p = 0. \tag{12}$$

2.3.5. Constant Temperature (CT) mode

The (spatially averaged) cell temperature $T_{avg}(t, \dot{y}(t), y(t))$ is a differential variable. The current time evolution forcing the cell temperature to a constant value can be obtained with the constraint

$$I(t, \dot{y}(t), y(t)) : \quad \frac{dT_{avg}}{dt}(t, \dot{y}(t), y(t)) = 0. \tag{13}$$

2.3.6. Constant electrolyte concentration (CCe) mode

The electrolyte lithium concentration $C_e(\upsilon, t, \dot{y}(t), y(t))$ is a differential variable; the current time evolution forcing the electrolyte concentration of the υth volume to a constant value can be obtained with the constraint

$$I(t, \dot{y}(t), y(t)) : \quad \frac{\partial C_e}{\partial t}(\upsilon, t, \dot{y}(t), y(t)) = 0. \tag{14}$$

2.3.7. Constant solid particle concentration (CCs) mode

The lithium concentration in the pth particle of the υth volume of the cell, $C_s(\upsilon, p, t, \dot{y}(t), y(t))$, is a differential variable. The current time evolution fixing it to a constant value can be obtained with the constraint

$$I(t, \dot{y}(t), y(t)) : \quad \frac{\partial C_s}{\partial t}(\upsilon, p, t, \dot{y}(t), y(t)) = 0. \tag{15}$$

2.4. Computation of safe fast charging protocols

The main goal of this work is the computation of safe, fast charging protocols for MPET models of lithium-ion batteries. This task can be formulated as a *dynamic optimization* [70,71] of the form

$$\min_{t_f, u(t)} J(t_f, \dot{y}(t_f), y(t_f)) \tag{16}$$

subject to

$$F(t, \dot{y}(t), y(t), u(t)) = 0 \tag{17}$$

$$S(t, \dot{y}(t), y(t), u(t)) \leq 0 \tag{18}$$

$$T(t_f, \dot{y}(t_f), y(t_f), u(t_f)) \leq 0 \qquad \forall\, 0 \leq t \leq t_f \tag{19}$$

where t_f is the final time, $u(t)$ is the control input, and $J(t_f, \dot{y}(t_f), y(t_f))$ is the objective function to be minimized, (17) is a set of (consistently initialized) DAEs defining the process model, (18) is a set of safety, path constraints,[1] and (19) is a set of terminal constraints. Ref. [70] suggests that optimal input directions can be classified as *constraint-seeking* or *sensitivity-seeking*. The constraint-seeking input directions push the system to the (path and terminal) constraints of the problem, while sensitivity-seeking input directions exploit the intrinsic compromises present in the system for optimizing the cost.

In the computation of optimal charging protocols, the terminal constraint and objective function account for the overall charging time (e.g., $J = t_f$, with t_f given by $\mathrm{SOC}(t_f) = \overline{\mathrm{SOC}}$ where $\overline{\mathrm{SOC}}$ is the desired state of charge to be reached), whereas path constraints are related to the safety of operations (e.g., upper bounds on current, voltage, power). In this scenario, a single signal (the current I) is available as control input, which plays the role of a *constraint-seeking* input [70]. According to the interpretation from [70], the optimal current should push the states of the system along the path constraints, which become activated one at a time, until the terminal constraint is met. This condition is stated formally as Assumption 1.

Assumption 1. Define switching times t_{sw} as the time instants in which the system transitions from one active constraint to the next:

$$\exists\, i_1, i_2 \text{ with } i_1 \neq i_2 \tag{20}$$

such that

$$S_{i_1}(t_{sw}^-, \dot{y}(t), y(t)) = 0 \text{ and } S_{i_2}(t_{sw}^-, \dot{y}(t), y(t)) \neq 0. \tag{21}$$

$$S_{i_1}(t_{sw}, \dot{y}(t), y(t)) = 0 \text{ and } S_{i_2}(t_{sw}, \dot{y}(t), y(t)) = 0. \tag{22}$$

$$S_{i_1}(t_{sw}^+, \dot{y}(t), y(t)) \neq 0 \text{ and } S_{i_2}(t_{sw}^+, \dot{y}(t), y(t)) = 0 \tag{23}$$

where S_i denotes the ith path constraint. Let $\mathcal{T}_{sw}$ be the set of switching times for the solution to the charging problem (16)–(19).

[1] In this work, the term *safe* denotes the fact that each computed protocol satisfies the associated set of safety constraints (18).

Assume that the optimal solution to the charging problem (16)–(19) satisfies the condition that, for each $t \in [0, t_f]$, $t \notin \mathcal{T}_{sw}$, there exists one and only one $i^*(t)$ such that $S_{i^*(t)}(t, \dot{y}(t), y(t)) = 0$.

In this scenario, the optimal solution is subdivided in time intervals in which a single constraint is active. Assumption 1 is supported by several results from the literature, where optimal charging protocols are obtained by solving an optimization problem [16,19–22]. A broader discussion of this point is deferred to Section 4.

While the optimal charging problem could be numerically solved with nonlinear programming tools [72,73], Assumption 1 allows for a more efficient approach, based on the concepts of *hybrid simulation* [69], and *general battery operating modes*, as discussed in Section 2.3. Assumption 1 implies that the optimal solution consists of a *sequence of battery operating modes*. The flowchart in Fig. 1(a) conceptually summarizes the algorithm adopted in this work for the solution of the optimal charging problem. Specifically, the desired safety and terminal constraints are set, and a battery simulation is started in the CC mode. The set of DAEs defining the battery model in CC mode are solved forward in time, until a new constraint is hit. In this case, the battery transitions to the operating mode associated with the new active constraint. The set of DAEs is thus tweaked by removing the CC mode constraint and including the new constraint associated with the desired operating mode, and the simulation is resumed. If a new constraint gets activated, the set of DAEs is set up accordingly. The process is repeated until the terminal constraint is hit. At that point, the simulation ends. If all constraints can be satisfied, and the simulation is correctly carried out until the end, the simulated current profile represents the proposed solution to the optimal charging problem. All the specified constraints may not be hit before reaching the terminal constraint.

This approach replaces the optimization by a *hybrid simulation*, in which the simulated system combines continuous dynamics, specified by a set of DAEs between each switch, with discontinuous switches, specified path constraints activation. This simulation can be implemented as a state transition network (STN) [68,69], for which each state corresponds to a specific operating mode of the battery, whereas the transition logic is defined by the activation of the associated constraints. An example is depicted in Fig. 1(b). An additional starting state, associated with zero current, is introduced to ensure numerical stability of the MPET simulation [34]. The current is then quickly ramped from zero to the CC state, consistently with the approach adopted in the considered MPET implementation [34]. The choice of CC as the first operating mode is motivated by the fact that, in absence of other path constraints, the optimal solution would require charging the battery at the maximum allowed current. If other constraints are present, this choice does not represent a limitation, since the battery can immediately switch to another operating mode as soon as a new constraint is hit. The current ramping at the beginning of the simulation is also useful in this context.

3. Results

The methodology discussed in the previous section is applied to a specific case study. Based on different safety constraints, several charging protocols are computed and analyzed to provide further insight for both the methodology and the specific protocol under consideration.

3.1. Case study

This work applies the above algorithm to an MPET model of A123 System's *APR18650M1A* LFP batteries [39]. The cells are characterized by a nominal capacity of 1.1 A/h, and a charge cut-off voltage of 3.6 V. Further details concerning the case study can be found in [74]. Details regarding the corresponding MPET model are given in the reminder of this section.

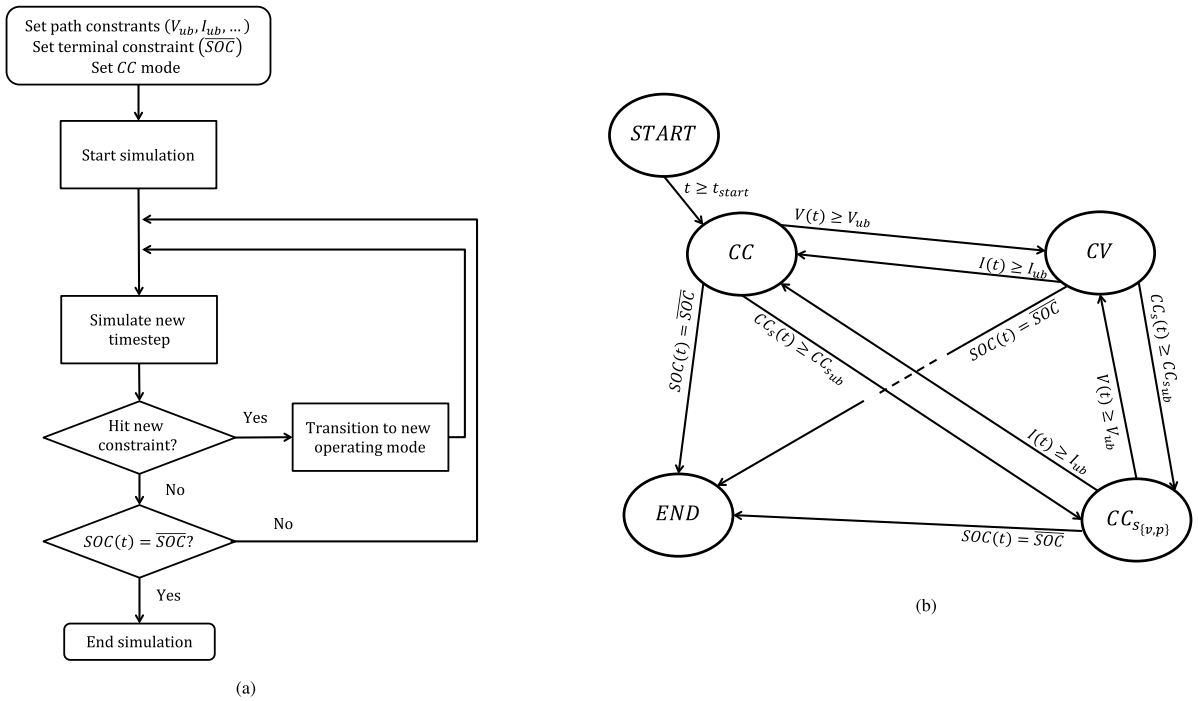

Fig. 1. Flowchart summarizing the algorithm for the solution of the optimal charging problem (a) and example of implementation as STN (b). $\overline{SOC}$ represents the desired state of charge at final time, while I_{ub}, V_{ub}, and $CC_{s_{ub}}$ represent upper bounds on current, voltage, and solid concentration, respectively.

Anode, cathode, and separator thicknesses are set to 38, 79, and 25 μm, respectively. Volume loading percents of active material for anode and cathode are 0.90 and 0.84, respectively. The porosities of the anode, cathode, and separator are 0.414, 0.562, and 0.4, respectively, and a Bruggeman exponent of −1.5 is assumed throughout. The anode and cathode are characterized by a bulk conductivity of 50 S and 0.1 S.

The anode and the cathode are discretized into 5 and 50 volumes, the separator is discretized in 5 volumes, 4 representative particles are used for each anode volume, and 2 representative particles are used for each cathode volume. Particles in the anode are modeled as spherical, with radii drawn from a Weibull distribution with mean 6 μm and standard deviation 2 μm; a CHR model is assumed for these particles [34]. Particles in the cathode are modeled as rectangular (approximating platelet particles), with thicknesses equal to 20 nm and main dimensions drawn from a lognormal distribution with mean and standard deviation equal to 100 nm and 20 nm; an ACR model is assumed for these particles [75].

Generalized BV kinetics [49] is considered for both electrodes, with a rate constant of 30 A/m^2 for the anode and 0.16 A/m^2 for the cathode. The anode kinetics is associated to film resistance set to 5 mΩ/m^2. For the plating reaction, a nucleation barrier 40 mV is estimated from experiments and experiencing the same film resistance as intercalation by assuming that plating occurs on the interface of SEI and graphite.

The functional forms defining free energy and chemical potential of anode and cathode active materials (LiC_6 and $LiFePO_4$) are given in SI. The electrolyte follows the full Stefan–Maxwell concentrated solution model, with parameters from [76,77], and an initial concentration of 1.067 kmol/m^3.

Finally, for non-isothermal modeling, the heat capacities of anode, cathode and separator are set to 700 J/(kg K). A heat transfer coefficient of 1 W/(m^2 K) is assumed for the separator. For the electrolyte thermal conductivity, [76] is again adopted as reference.

The simulated and experimentally measured voltage profiles from [74] (Supplementary Fig. 27) are compared in the SI. The comparison highlights that the proposed model can reasonably capture the experimental voltage trend for charging operations carried out at constant current, ranging from $C/10$ up to $8C$.

Remark. A fine spatial discretization of the cell should be used to reduce numerical artifacts in solution of the associated set of DAEs. Numerical oscillations affecting the solution may erroneously trigger an active constraint switch, and in turn result in oscillations in the charging protocol. Volume discretization is limited by the size of particles, which need to be fully contained in each volume. In this work, a fine discretization can be used for cathode, whereas anode discretization is limited to few volumes. To reduce the risk of constraint activations due to numerical artifacts, a small tolerance on constraint activation is assumed for all constraints. Each tolerance is proportional to the constraint value. In this work, tolerances are specified as a percentage, and the same tolerance percentage value is applied to all constraints. Constraint-specific values could also be introduced. Starting from zero tolerance, the value was progressively increased until a feasible solution with no or minor protocol oscillations was achieved.

Based on the battery operating modes defined in Section 2.3, five different protocols are computed and discussed in the reminder of this section. Table 1 summarizes the main features of each protocol, as well as the time required for its computation by means of a Intel® Core™ 2.60 GHz i7-6700HQ CPU. The computation of each protocol requires solving a system of 758 DAEs. Figs. 2–5 and 7 plot the dynamics of the states of interest (state of charge, voltage, current, power, lithium-plating overpotential, average cell temperature, electrolyte concentration, and solid particle concentration) for each protocol. In the analysis of results, particular focus is placed on lithium-plating overpotential and average cell temperature, which are typically accounted as responsible for battery performance degradation [37]. To preserve battery lifetime, the lithium-plating overpotential should not reach negative values, and the cell temperature should not increase too much during charge operations.

Table 1
Main features of the charging protocols and associated computation times. Each simulation requires the solution of a system of 758 DAEs.

Protocol	Mode 1 Duration [s]	Mode 2 Duration [s]	Mode 3 Duration [s]	Charging Time [s]	Computation Time [s]
CC-CV	CC(111.22)	CV(678.85)	N/A	790.07	414.95
CC-CP-CV	CC(2.28)	CP(332.08)	CV527.43)	861.79	412.21
CC-CT-CV	CC(98.78)	CT(194.57)	CV(535.71)	829.06	412.16
CC-CV-CLO	CC(111.96)	CV(420.44)	CLO(225.43)	757.83	378.07
CC-CSe-CV	CC(5.64)	CCe(1686.02)	CCs(227.49)	1919.15	611.82

3.2. Current and voltage constraints

The first protocol design scenario analyzed in this work consists of the standard approach of having upper bounds on the current and voltage. The algorithm in Section 2.4 is used to compute a safe, fast charging protocol as the solution of the dynamic optimization

$$\min_{t_f} \; t_f \tag{24}$$

subject to

$$F(t, \dot{y}(t), y(t)) = 0 \tag{25}$$
$$I(t) \leq 8C \tag{26}$$
$$V(t) \leq 3.6 \text{ V} \tag{27}$$
$$\text{SOC}(t_f) = 0.8 \tag{28}$$
$$\forall\, 0 \leq t \leq t_f$$

with a 1% tolerance on constraint activation. Initially the current quickly ramps to its upper limit for a CC phase, which lasts until voltage reaches its upper limit (Fig. 2). At this point, a CV phase begins, with current decaying towards zero with an exponential trend. The low frequency oscillations can be attributed to the multiphase battery physics, and small amplitude, high-frequency oscillations can be attributed to numerical artifacts. A single switch occurs between CC and CV phases, due to the presence of the 1% tolerance on constraint activation.

The resulting charging protocol is a CC-CV approach, with an overall charging time of 790.07 s. The specific duration of each phase is reported in Table 1. The solution was obtained in 414.95 s.

3.3. Current, voltage and power constraints

The second protocol design scenario analyzed in this work consists of upper bounds on the current, voltage, and power. A safe, fast charging protocol is then computed as the solution of the dynamic optimization

$$\min_{t_f} \; t_f \tag{29}$$

subject to

$$F(t, \dot{y}(t), y(t)) = 0 \tag{30}$$
$$I(t) \leq 8C \tag{31}$$
$$V(t) \leq 3.6 \text{ V} \tag{32}$$
$$P(t) \leq 270 \text{ W/m}^2 \tag{33}$$
$$\text{SOC}(t_f) = 0.8 \tag{34}$$
$$\forall\, 0 \leq t \leq t_f$$

with a 3% tolerance on constraint activation. Initially the current quickly ramps to its upper limit for a CC phase, which lasts for few instants only, as the power bound is immediately hit (Fig. 3). In the CP phase, the current settles at about 5C, and slowly varies so as to compensate for voltage oscillations and guarantee constant, maximum power. Then, voltage hits its upper bound and a CV phase concludes the charging operations. Specifically, during this last CV phase, the current decays exponentially. The presence of high-frequency artifacts is well tolerated due to the presence of the 3% tolerance on constraint activation.

The overall charging protocol consists of a CC-CP-CV approach, with an overall charging time of 861.79 s. The specific duration of each phase is reported in Table 1. The solution was obtained in 412.21 s.

A comparison with the previous scenario highlights that the implementation of an upper bound on power can reduce the temperature increase associated with charging operations (cf., Figs. 2 and 3), at the cost of a longer charging time. In both cases, a negative lithium-plating overpotential is reached towards the end of charging operations.

3.4. Current, voltage, and temperature constraints

The third protocol design scenario analyzed in this work consists of upper bounds on the current, voltage, and average cell temperature. This approach is particularly interesting since excessive heating shortens battery lifetime. A safe, fast charging protocol is computed as the solution of the dynamic optimization

$$\min_{t_f} \; t_f \tag{35}$$

subject to

$$F(t, \dot{y}(t), y(t)) = 0 \tag{36}$$
$$I(t) \leq 8C \tag{37}$$
$$V(t) \leq 3.6 \text{ V} \tag{38}$$
$$T_{avg}(t) \leq 310 \text{ K} \tag{39}$$
$$\text{SOC}(t_f) = 0.8 \tag{40}$$
$$\forall\, 0 \leq t \leq t_f$$

with a 1% tolerance on constraint activation. The solution is characterized by an initial CC phase, followed by a CT phase and a final CV phase (Fig. 4). At the switching between the CC and CT phases, the current immediately drops from its maximum value to about $5C$, then exponentially decreases during the CV phase, as in the previous scenarios. Similarly, voltage and power show a sudden decease in correspondence to the CC/CV switching.

The overall charging protocol consists of a CC-CT-CV approach, with an overall charging time of 829.06 s. The specific duration of each phase is reported in Table 1. The solution was obtained in 412.16 s.

In this scenario, temperature increase during charging operations is directly limited by the explicit upper bound on temperature. While the maximum temperature reached during charge is similar to that associated with the CC-CP-CV protocol, a shorter charging time is achieved. The shorter charging occurs because the current and temperature are held at their maximum during charge operations, which could not occur in the previous scenarios due to its constraint on the maximum allowed power. A negative lithium-plating overpotential is reached during the last 200 s of charging operations.

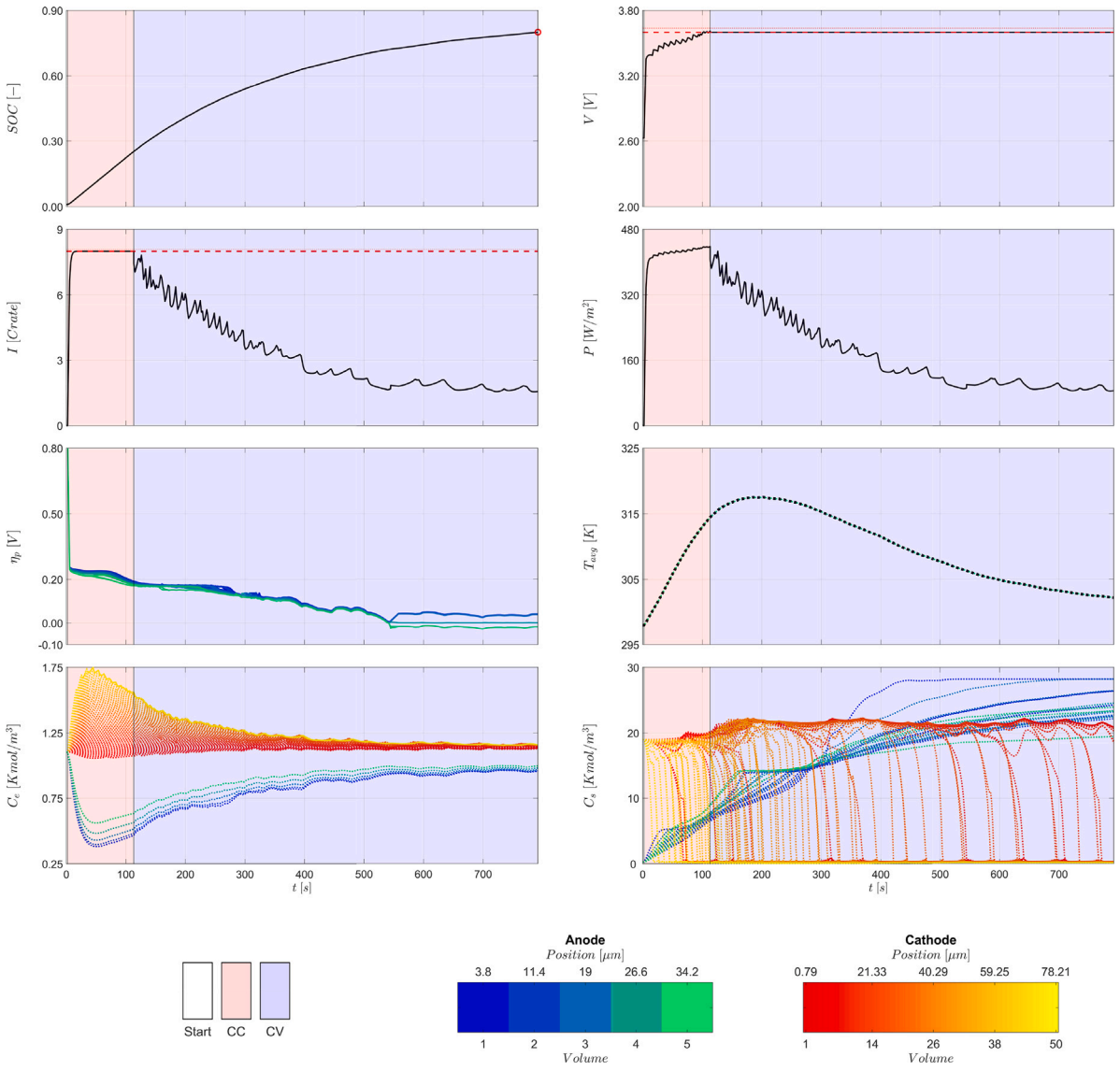

Fig. 2. CC-CV Protocol. Time evolution of the main states of the battery (SOC, voltage V, current I, power P, lithium-plating overpotential η_p, spatially averaged cell temperature T_{avg}, electrolyte concentration C_e, and solid particle concentration C_s). Nominal constraints are depicted as thick red, dashed lines. Constraints relaxed including a 1% deadband are depicted as thin, red dotted lines. (For interpretation of the references to color in this figure legend, the reader is referred to the web version of this article.)

3.5. Current, voltage, and lithium-plating overpotential constraints

The fourth protocol design scenario analyzed in this work consists of upper bounds on the current and voltage, and a lower bound on the lithium-plating overpotential. Negative lithium-plating overpotential values typically trigger side reactions which eventually degrade the battery lifetime. A proper choice of the corresponding lower bound can help prevent this degradation mechanism from occurring. In the protocol computation, the lower bound for lithium-plating overpotential is conservatively constrained to 0.01 V, to avoid the onset of plating reactions. The corresponding safe, fast charging protocol is computed as the solution of the dynamic optimization

$$\min_{t_f} \; t_f \tag{41}$$

subject to

$$F(t, \dot{y}(t), y(t)) = 0 \tag{42}$$

$$I(t) \leq 8C \tag{43}$$

$$V(t) \leq 3.6 \text{ V} \tag{44}$$

$$\eta_p(t, v_a, p_a) \geq 0.01 \text{ V} \tag{45}$$

$$\text{SOC}(t_f) = 0.8 \tag{46}$$

$$\forall\, 0 \leq t \leq t_f$$

$$v_a = 5$$

$$p_a = 1, 2, 3, 4$$

with a 3% tolerance on constraint activation. In this problem formulation, the lower bound on lithium-plating overpotential applies to all the particles in the last volume of the anode (i.e., at the anode/separator interface). The solution coincides with that of the standard CC-CV protocol until the lower bound on the lithium-plating overpotential is hit (at about $t = 531$ s), and a CLO phase is triggered (Fig. 5). This last phase replaces part of the original CV phase of the CC-CV protocol. Up to this point, the two solutions have similar current profiles.

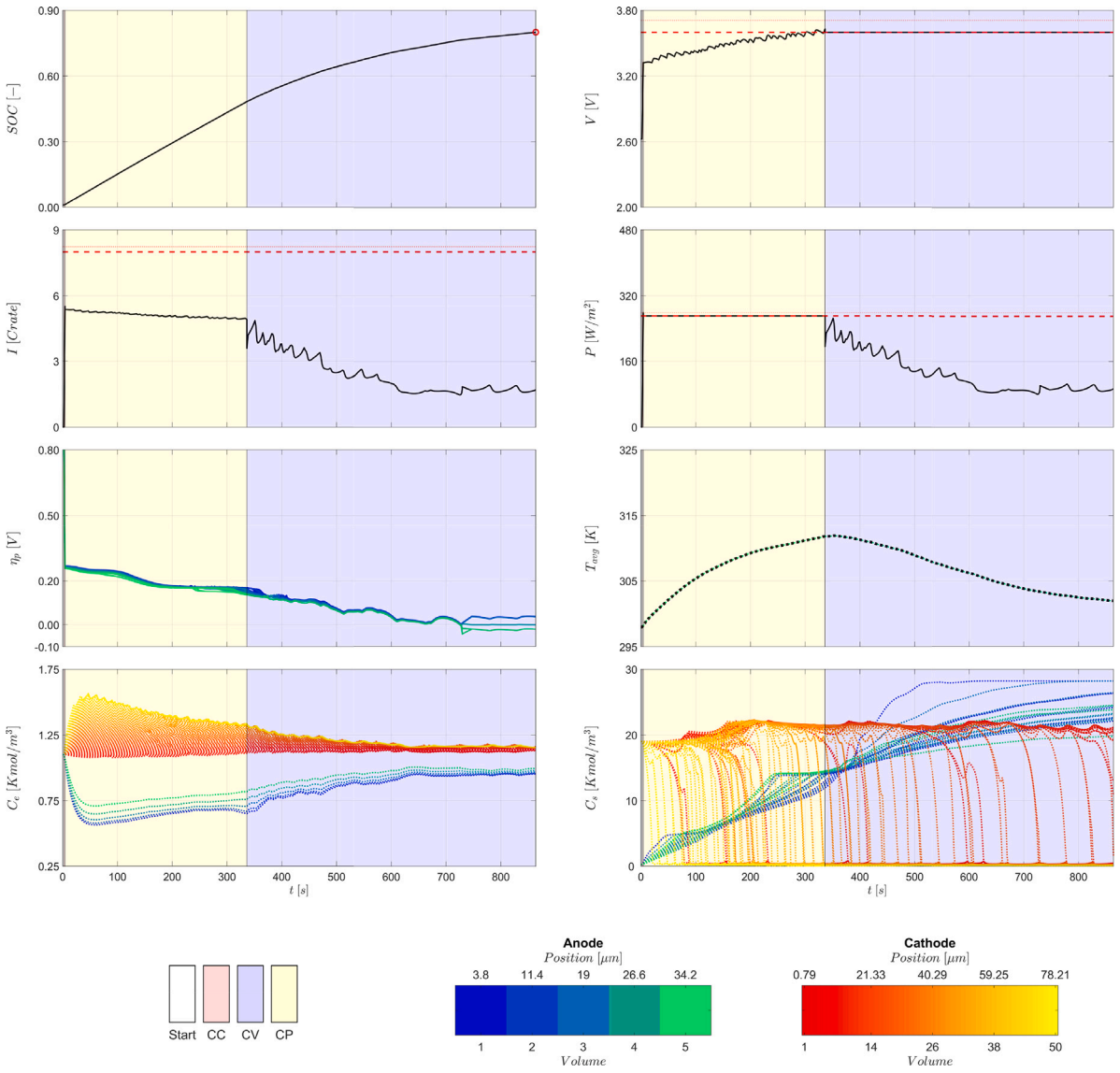

Fig. 3. CC-CP-CV Protocol. Time evolution of the main states of the battery (SOC, voltage V, current I, power P, lithium-plating overpotential η_p, spatially averaged cell temperature T_{avg}, electrolyte concentration C_e, and solid particle concentration C_s). Nominal constraints are depicted as thick red, dashed lines. Constraints relaxed including a 3% deadband are depicted as thin, red dotted lines. (For interpretation of the references to color in this figure legend, the reader is referred to the web version of this article.)

The overall charging protocol consists of a CC-CV-CLO approach, with an overall charging time of 757.83 s. The specific duration of each phase is reported in Table 1. The solution was obtained in 378.07 s.

While lithium-plating side reactions can be limited by explicitly forcing the lower bound on lithium-plating overpotential, the maximum temperature reached during charge operations coincides with that of the CC-CV protocol. To achieve both results for this case study, it would then be necessary to explicitly consider both bounds in the optimization defining the charging protocol.

3.6. Current, voltage, and electrolyte conductivity constraints

The last protocol design scenario analyzed in this work consists of upper bounds on the current and voltage, and a lower bound on the electrolyte conductivity $\sigma_e(t, v_a, v_c)$ in each volume of both anode and cathode. Moreover, an upper bound on solid particle concentration $C_s(t, v_a, p_a)$ is also imposed to the anode. The corresponding safe, fast charging protocol could be obtained as the solution of the dynamic optimization

$$\min_{t_f} \; t_f \tag{47}$$

subject to

$$F(t, \dot{y}(t), y(t)) = 0 \tag{48}$$

$$I(t) \leq 8C \tag{49}$$

$$V(t) \leq 3.6 \text{ V} \tag{50}$$

$$\sigma_e(t, v_a, v_c) \geq 1.1 \text{ S/m} \tag{51}$$

$$C_s(t, v_a, p_a) \leq 27940 \text{ mol/m}^3 \tag{52}$$

$$\text{SOC}(t_f) = 0.8 \tag{53}$$

$$\forall\, 0 \leq t \leq t_f$$

$$v_a = 1, 2, \ldots, 5$$

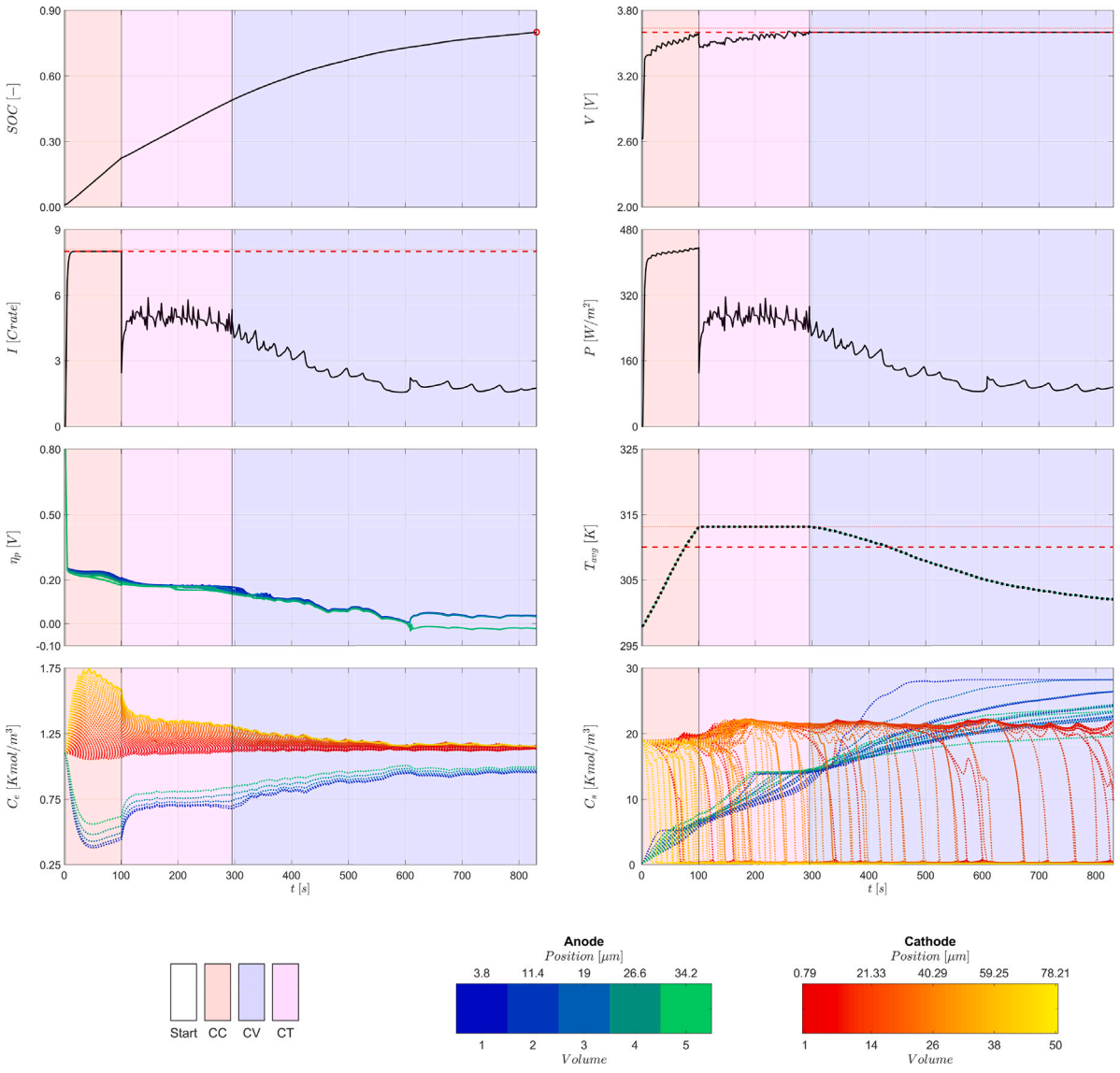

Fig. 4. CC-CT-CV Protocol. Time evolution of the main states of the battery (SOC, voltage V, current I, power P, lithium-plating overpotential η_p, spatially averaged cell temperature T_{avg}, electrolyte concentration C_e, and solid particle concentration C_s). Nominal constraints are depicted as thick red, dashed lines. Constraints relaxed including a 1% deadband are depicted as thin, red dotted lines. (For interpretation of the references to color in this figure legend, the reader is referred to the web version of this article.)

$$v_c = 1, 2, \dots, 50$$
$$p_a = 1, 2, 3, 4$$

with a 1% tolerance on constraint activation. The electrolyte conductivity mainly depends on electrolyte concentration and temperature. Assuming limited variations of temperature during charge operations, and assuming knowledge of the expression relating electrolyte conductivity to electrolyte concentration, upper and lower bounds on electrolyte concentration can be derived corresponding to the original bound on electrolyte conductivity.[2] Constraint (51) can then be replaced by the set of constraints:

$$T_{avg}(t) \leq 310 \text{ K} \tag{54}$$

$$C_e(t, v_a, v_c) \leq 1350 \text{ mol/m}^3 \tag{55}$$

$$C_e(t, v_a, v_c) \geq 930 \text{ mol/m}^3 \quad \forall\, v_a = 1, 2, \dots, 5,\ v_c = 1, 2, \dots, 50. \tag{56}$$

Concentration constraints are derived from the curve depicted in Fig. 6. Initially the current ramps to its maximum value and the system almost immediately hits a different constraint (Fig. 7). In this case, the lower bound on electrolyte concentration is hit, and the system transitions to the CCe operating mode. The current very quickly drops from its maximum value and fluctuates around 2C to maintain a constant minimum electrolyte concentration. Charging operations are instead concluded with a brief CCs phase, triggered by the corresponding constraint activation at about 1700 s. Both upper bounds on temperature electrolyte concentration are never reached during the simulation.

The overall charging protocol consists of a CC-CCe-CCs approach, with an overall charging time of 1919.15 s. The specific duration of each phase is reported in Table 1. The solution was obtained in 611.82 s. In

[2] A limit on the maximum temperature variation could also be explicitly introduced into the optimization, as discussed earlier in this article.

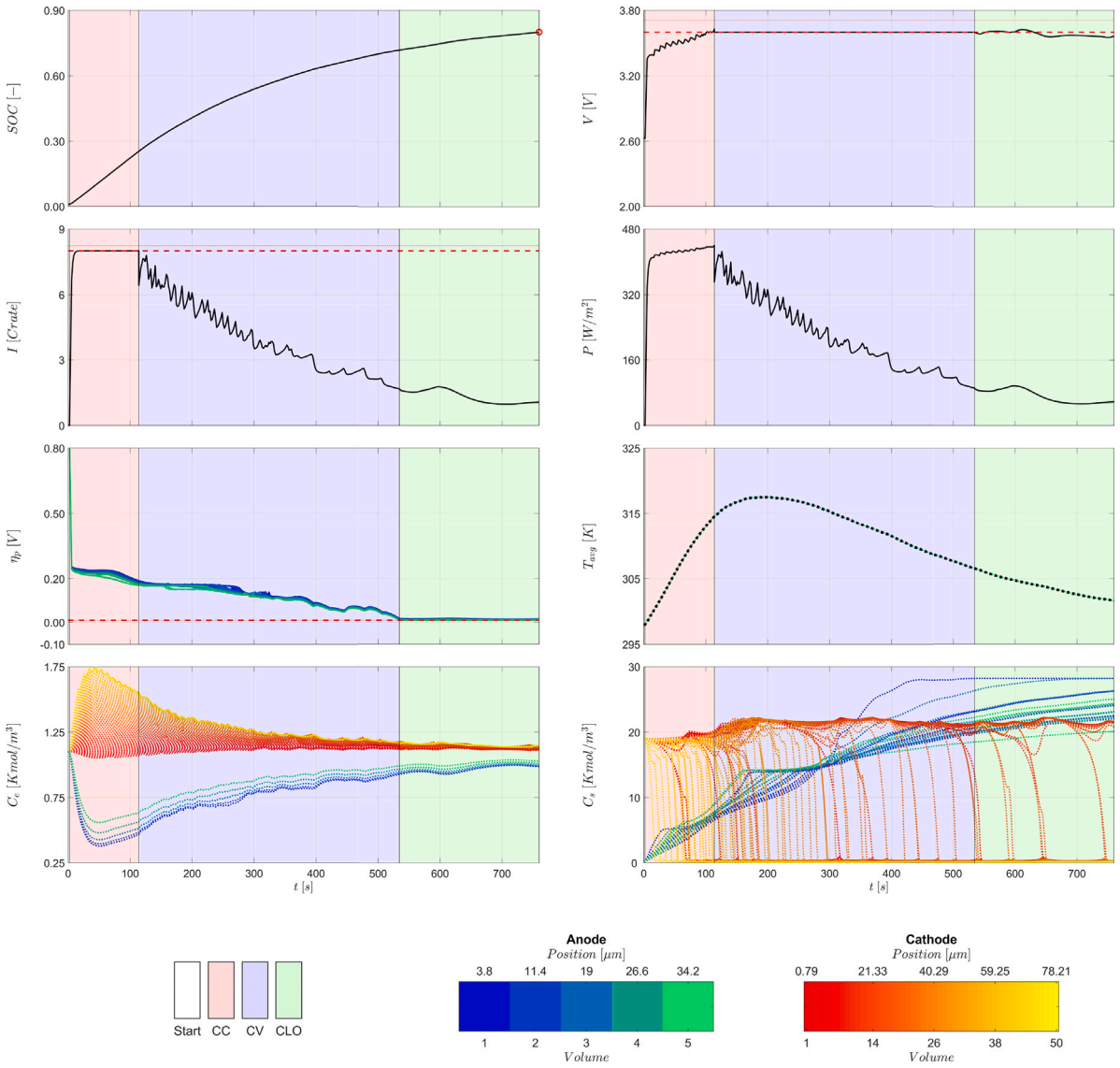

Fig. 5. CC-CV-CLO Protocol. Time evolution of the main states of the battery (SOC, voltage V, current I, power P, lithium-plating overpotential η_p, spatially averaged cell temperature T_{avg}, electrolyte concentration C_e, and solid particle concentration C_s). Nominal constraints are depicted as thick red, dashed lines. Constraints relaxed including a 3% deadband are depicted as thin, red dotted lines. (For interpretation of the references to color in this figure legend, the reader is referred to the web version of this article.)

this scenario, the lithium-plating overpotential never falls to negative values. Moreover, temperature shows only a small increase during charge operations. However, the charging time results much longer than in the previous scenarios, as charging operations are conducted at relatively low current, as shown in Fig. 7.

4. Discussion

The results presented and analyzed in the previous section highlight the efficiency of the proposed approach for the design of safe, fast charging protocols for multiphase batteries. Specifically, the protocol design problem is formulated as a dynamic optimization, and a feasible solution is found by embedding the constraints into the battery model (Sections 2.3 and 2.4). With this methodology, a feasible solution to the optimal charging problem can be found with a computation time of few minutes, despite the complexity of the multiphase battery model, its fine cathode discretization, and the presence of multiple particles per volume. As already introduced in Section 2.4, the proposed approach guarantees feasibility of the solution, but only guarantees its optimality if Assumption 1 holds. While an analytical proof of optimality is beyond the scope of this work, and is left as future development, it is important to underline that many results reported in the literature support Assumption 1 as being exactly or approximately true for lithium-ion batteries. As notable examples, a nonlinear MPC (NMPC) is used in [19] to fast charge a cell while avoiding large currents, voltages, and negative lithium-plating overpotentials in the anode. The resulting solution closely resembles a CC-CV-CLO profile. In [20], MPC is used to fast charge a cell while satisfying constraints on current, temperature, and electrolyte/solid surface concentrations. In this case, the solution resembles a CC-CCe-CT-CCs profile. A sensitivity-based MPC is developed in [21] to fast charge a battery pack, resulting in a CC-CT-CV profile. Moreover, CC-CCs and CC-CCe-CCs profiles are recovered in [22]. A CC-CV-CLO-CMS-CT profile is instead obtained in [16] (where CMS denotes Constant Mechanical Stress).

A common approach to solve protocol design problems (i.e., optimal control problems involving DAEs) is *control vector parametrization* [72]. This technique requires choosing *a priori* a parametrization for the control signal (typically, piecewise constant over time intervals of predefined length, resulting in a discrete-time approximation of the continuous-time solution). Restricting the search space by applying a predefined parametrization simplifies the optimization but the results

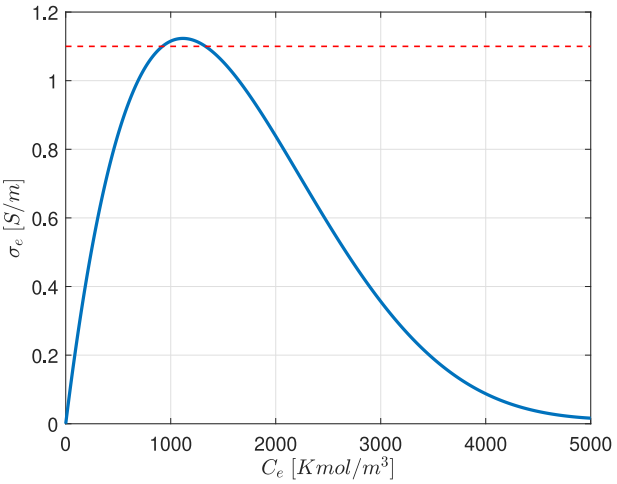

Fig. 6. Electrolyte conductivity as function of electrolyte concentration for constant temperature $T = 298$ K (blue, solid line) and lower bound on electrolyte conductivity (red, dashed line). (For interpretation of the references to color in this figure legend, the reader is referred to the web version of this article.)

can be suboptimal since the entire search space is no longer available. Another approach to numerically solve for an optimal protocol explicitly considers the *optimality conditions* associated with the optimal control problem in the numerical calculation [70,71]. This approach does not introduce any suboptimality, but is computationally expensive and not suitable for online implementation. For complex models such as MPET, the computation of the optimally conditions themselves may be rather involved. The approach based on mixed continuous-discrete simulation adopted in this article is an intermediate solution. On one hand, the search space – introduced with Assumption 1 – is restricted, based on both theoretical and practical considerations. On the other hand, the computational complexity required to solve the optimization is greatly reduced, from that of an optimization to that of a simulation. The results indicate that the obtained control action (current) can evolve very rapidly, and with arbitrary shapes, to ensure constraint satisfaction and fast charging times. In addition, the time required to solve the optimizations is reasonable, consistent with possible online implementations of the approach.

As apparent from the above literature review, MPC is a further tool explored in the literature for the design of safe, fast charging protocols. It is therefore interesting to discuss advantages and disadvantages of the approach adopted in this work compared to MPC. At each time instant, an MPC algorithm solves a (possibly non-convex) constrained optimal control problem, and determines an optimal input sequence. Only the first element of the optimal input sequence is actually applied to the plant (i.e., the receding horizon principle), and the optimal control problem is solved again at the following time instant, with updated initial conditions [78]. Solving an optimal control problem may require a very large number of function evaluations. Moreover, a solution must be computed within the controller sampling time, thus making MPC schemes very demanding in term of computing power. On the contrary, the approach proposed in this work embeds the dynamical optimization in an augmented formulation of the process model itself. By doing so, the optimization is turned into a nonlinear root finding problem, which has several advantages:

- nonlinear root finding is much less expensive than optimization;
- adaptive time-stepping algorithms in DAE solvers directly handle stiffness compared to constant time steps commonly used in MPC;
- path constraints are satisfied at all times within absolute and relative tolerances.

On the other hand, MPC schemes provide some robustness to modeling uncertainties, in view of the receding horizon principle. The solutions obtained in this work are instead nominal, open-loop, thus sensitive to modeling uncertainties. However, simple closed-loop control schemes can be designed to track the open-loop solutions, which are therefore used as Ref. [79]. Furthermore, it is important to underline that, thanks to its extremely reduced computational complexity, a receding horizon implementation of the approach adopted in this work would be viable, even in presence of complex battery models such as MPET ones. A comparison of charging times and protocol computation times (see Table 1) supports this claim. Moreover, depending on the specific case study, it may be possible to reduce the number of volumes in the electrode discretization and compensate for possible artifacts by increasing the tolerance on constraint activation to further reduce the computational complexity of the problem.

Additionally, due to the open-loop nature of the charging protocols computed in this work, no guarantee can be given in terms of *robust* constraint satisfaction. This uncertainty should be carefully accounted for during the design phase of the protocol, by including some *backoff* in the definition of safety constraints [70,71]. The idea is implementing a tightened set of constraints to account for possible model uncertainties. In this way, some degree of robustness is provided for the satisfaction of the original set of constraints, possibly at the price of a reduced optimality. In this context, recall that the MPET model, on top of which the charging protocols are computed, allows for an accurate description of the battery dynamics, even in presence of multiphase materials. It is therefore reasonable to expect that the backoff required using a properly calibrated MPET model could be lower than required by standard PET, or by even simpler models such as reduced-order or equivalent circuit ones. The MPET model may also be more likely to reproduce – and be trained to avoid – subtle voltage features related to degradation, such as those recently associated with the onset of lithium plating in graphite electrodes [61].

A final remark concerns possible future developments of this work. On one hand, advances in MPET modeling may include a detailed description of battery aging processes. Such advances could be exploited for the design of fast charging protocols by considering lifetime-specific operating modes, and for the evaluation of the protocol's performance over a number of cycling conditions [80]. On the other hand, a more theoretical analysis could be useful to derive formal proofs of optimality for the protocols computed via hybrid simulation or, in case this will not result possible, to quantify the sub-optimality affecting these solutions.

5. Conclusions

This work explores a methodology for an efficient computation of safe, fast charging protocols for batteries composed of multiphase materials. The protocol design problem is typically formulated and solved as an optimization problem. The proposed approach instead interprets a charging protocol as a sequence of general battery operating modes (such as constant current, voltage, power, lithium-plating overpotential) and solves the protocol design problem by means of a single, hybrid simulation. This efficient approach allows leveraging very detailed battery models, which would otherwise be intractable for online implementations. This work deals with the presence of multiphase materials, by exploiting MPET, which enhances the description of several phenomena not properly captured by standard PET. The methodology is applied to an MPET model of a commercially available LFP battery, and different protocols are derived and compared to highlight the effectiveness of the approach, as well as specific advantages and disadvantages of each protocol. While the use of a specific multiphase model in the computation of charging protocols alone represents a novelty in the literature, its combination with the concept of a general battery operating mode, and the application of the proposed methodology to a LFP case study model represent the main contributions of this work.

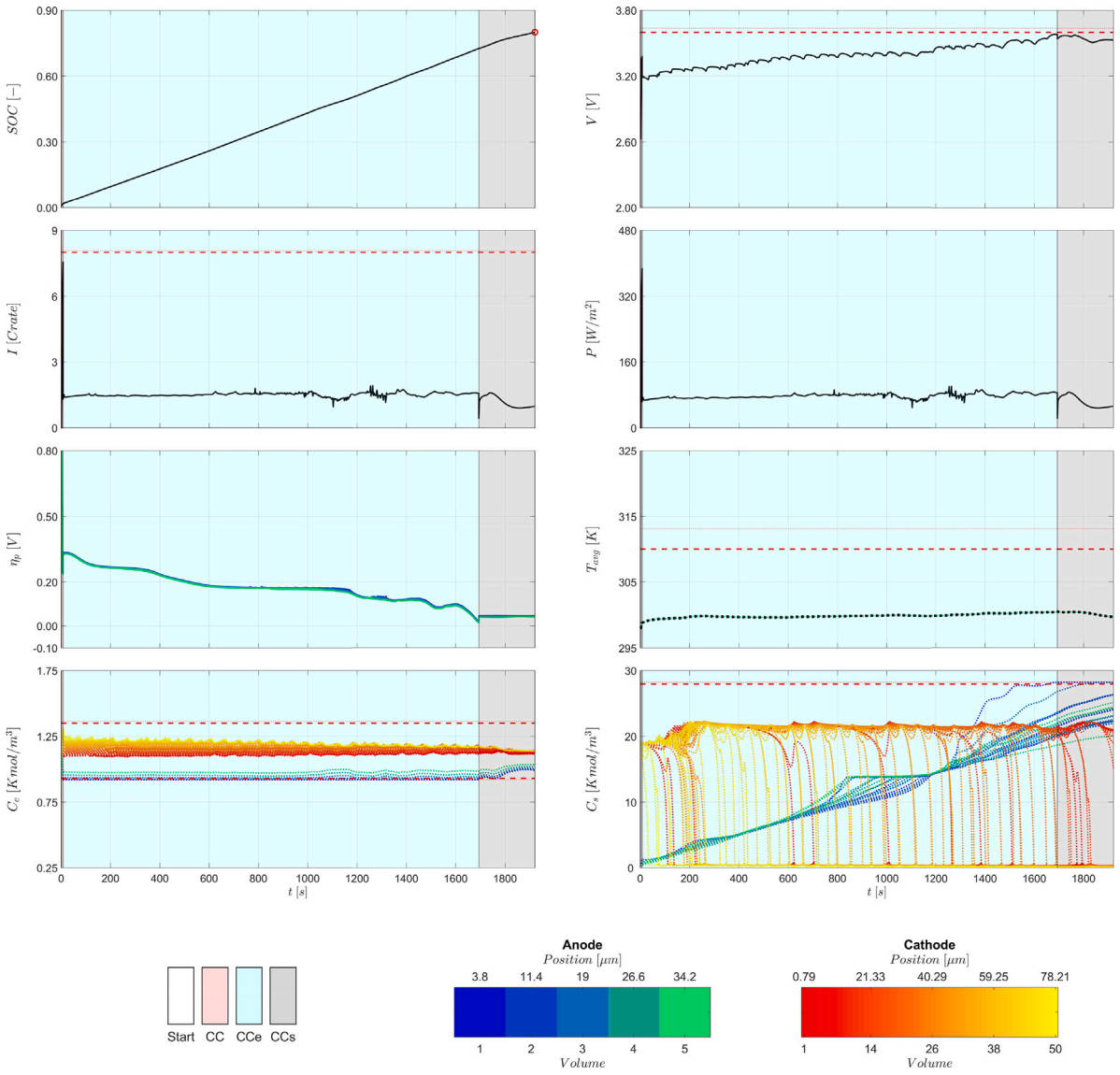

Fig. 7. CC-CSe-CCs Protocol. Time evolution of the main states of the battery (SOC, voltage V, current I, power P, lithium-plating overpotential η_p, spatially averaged cell temperature T_{avg}, electrolyte concentration C_e, and solid particle concentration C_s). Nominal constraints are depicted as thick red, dashed lines. Constraints relaxed including a 1% deadband are depicted as thin, red dotted lines. (For interpretation of the references to color in this figure legend, the reader is referred to the web version of this article.)

CRediT authorship contribution statement

Giacomo Galuppini: Conceptualization, Data curation, Formal analysis, Methodology, Software, Validation, Visualization, Writing – original draft, Writing – review & editing. **Marc D. Berliner:** Conceptualization, Formal analysis, Methodology, Writing – original draft, Writing – review & editing. **Huada Lian:** Data curation, Software, Validation, Visualization, Writing – original draft, Writing – review & editing. **Debbie Zhuang:** Data curation, Software, Validation, Visualization, Writing – original draft, Writing – review & editing. **Martin Z. Bazant:** Funding acquisition, Project administration, Resources, Supervision, Writing – original draft, Writing – review & editing. **Richard D. Braatz:** Conceptualization, Funding acquisition, Methodology, Project administration, Resources, Supervision, Writing – original draft, Writing – review & editing.

Declaration of competing interest

The authors declare that they have no known competing financial interests or personal relationships that could have appeared to influence the work reported in this paper.

Data availability

The code will be made available on github.

Acknowledgments

The authors would like to acknowledge Peter Weddle, Tyler Evans, Robert J. Kee, and Tyrone L. Vincent from Colorado School of Mines for providing some initial parameter estimates and experimental data.

Funding

This work was supported by the Toyota Research Institute through the D3BATT Center on Data-Driven-Design of Rechargeable Batteries.

Code availability

All the software code related to this work is available online at https://github.com/GiacomoGaluppini?tab=repositories.

Appendix A. Supplementary data

Supplementary material related to this article can be found online at https://doi.org/10.1016/j.jpowsour.2023.233272.

References

[1] B. Dunn, H. Kamath, J.-M. Tarascon, Electrical energy storage for the grid: A battery of choices, Science 334 (6058) (2011) 928–935.

[2] C. Chen, F. Shang, M. Salameh, M. Krishnamurthy, Challenges and advancements in fast charging solutions for EVs: A technological review, in: IEEE Transportation Electrification Conference and Expo, 2018, pp. 695–701.

[3] L. Lu, X. Han, J. Li, J. Hua, M. Ouyang, A review on the key issues for lithium-ion battery management in electric vehicles, J. Power Sources 226 (2013) 272–288.

[4] J. Tarascon, M. Armand, Issues and challenges facing rechargeable lithium batteries, Nature 414 (6861) (2011) 359–367.

[5] S. Ahmed, I. Bloom, A.N. Jansen, T. Tanim, E.J. Dufek, A. Pesaran, A. Burnham, R.B. Carlson, F. Dias, K. Hardy, M. Keyser, C. Kreuzer, A. Markel, A. Meintz, C. Michelbacher, M. Mohanpurkar, P.A. Nelson, D.C. Robertson, D. Scoffield, M. Shirk, T. Stephens, R. Vijayagopal, J. Zhang, Enabling fast charging–A battery technology gap assessment, J. Power Sources 367 (2017) 250–262.

[6] D. Anseán, M. González, J. Viera, V. García, C. Blanco, M. Valledor, Fast charging technique for high power lithium iron phosphate batteries: A cycle life analysis, J. Power Sources 239 (2013) 9–15.

[7] A. Tomaszewska, Z. Chu, X. Feng, S. O'Kane, X. Liu, J. Chen, C. Ji, E. Endler, R. Li, L. Liu, Y. Li, S. Zheng, S. Vetterlein, M. Gao, J. Du, M. Parkes, M. Ouyang, M. Marinescu, G. Offer, B. Wu, Lithium-ion battery fast charging: A review, ETransportation 1 (2019) 100011.

[8] M. Xu, X. Wang, L. Zhang, P. Zhao, Comparison of the effect of linear and two-step fast charging protocols on degradation of lithium-ion batteries, Energy 227 (2021) 120417.

[9] M. Xu, R. Wang, B. Reichman, X. Wang, Modeling the effect of two-stage fast charging protocol on thermal behavior and charging energy efficiency of lithium-ion batteries, J. Energy Storage 20 (2018) 298–309.

[10] R. Mathieu, O. Briat, P. Gyan, J.-M. Vinassa, Comparison of the impact of fast charging on the cycle life of three lithium-ion cells under several parameters of charge protocol and temperatures, Appl. Energy 283 (2021) 116344.

[11] D. Anseán, M. Dubarry, A. Devie, B. Liaw, V. García, J. Viera, M. González, Fast charging technique for high power $LiFePO_4$ batteries: A mechanistic analysis of aging, J. Power Sources 321 (2016) 201–209.

[12] D.P. Finegan, A. Quinn, D.S. Wragg, A.M. Colclasure, X. Lu, C. Tan, T.M. Heenan, R. Jervis, D.J. Brett, S. Das, T. Gao, D.A. Cogswell, M.Z. Bazant, M. Di Michiel, S. Checchia, P.R. Shearing, K. Smith, Spatial dynamics of lithiation and lithium plating during high-rate operation of graphite electrodes, Energy Environ. Sci. 13 (8) (2020) 2570–2584.

[13] P. Kollmeyer, A. Hackl, A. Emadi, Li-ion battery model performance for automotive drive cycles with current pulse and EIS parameterization, in: IEEE Transportation Electrification Conference and Expo, 2017, pp. 486–492.

[14] P.H.L. Notten, B. Op het Veld, J.R.G. Van Beek, Boostcharging Li-ion batteries: A challenging new charging concept, J. Power Sources 145 (1) (2005) 89–94.

[15] N.A. Chaturvedi, R. Klein, J. Christensen, J. Ahmed, A. Kojic, Algorithms for advanced battery-management systems, IEEE Control Syst. Mag. 30 (3) (2010) 49–68.

[16] P. Mohtat, S. Pannala, V. Sulzer, J.B. Siegel, A.G. Stefanopoulou, An algorithmic safety VEST for Li-ion batteries during fast charging, IFAC-PapersOnLine 54 (20) (2021) 522–527.

[17] M. Xu, R. Wang, P. Zhao, X. Wang, Fast charging optimization for lithium-ion batteries based on dynamic programming algorithm and electrochemical-thermal-capacity fade coupled model, J. Power Sources 438 (2019) 227015.

[18] P. Nambisan, P. Saha, M. Khanra, Real-time optimal fast charging of Li-ion batteries with varying temperature and charging behaviour constraints, J. Energy Storage 41 (2021) 102918.

[19] S. Kolluri, S.V. Aduru, M. Pathak, R.D. Braatz, V.R. Subramanian, Real-time nonlinear model predictive control (NMPC) strategies using physics-based models for advanced lithium-ion battery management system (BMS), J. Electrochem. Soc. 167 (6) (2020) 063505.

[20] C. Zou, C. Manzie, D. Nešić, Model predictive control for lithium-ion battery optimal charging, IEEE/ASME Trans. Mechatronics 23 (2) (2018) 947–957.

[21] A. Pozzi, M. Torchio, R.D. Braatz, D.M. Raimondo, Optimal charging of an electric vehicle battery pack: A real-time sensitivity-based model predictive control approach, J. Power Sources 461 (2020) 228133.

[22] H. Perez, S. Dey, X. Hu, S. Moura, Optimal charging of li-ion batteries via a single particle model with electrolyte and thermal dynamics, J. Electrochem. Soc. 164 (7) (2017) A1679–A1687.

[23] P.M. Attia, A. Grover, N. Jin, K.A. Severson, T.M. Markov, Y.-H. Liao, M.H. Chen, B. Cheong, N. Perkins, Z. Yang, P.K. Herring, M. Aykol, S.J. Harris, R.D. Braatz, S. Ermon, W.C. Chueh, Closed-loop optimization of fast-charging protocols for batteries with machine learning, Nature 578 (7795) (2020) 397–402.

[24] B. Jiang, M.D. Berliner, K. Lai, P.A. Asinger, H. Zhao, P.K. Herring, M.Z. Bazant, R.D. Braatz, Fast charging design for lithium-ion batteries via Bayesian optimization, Appl. Energy 307 (2022) 118244.

[25] J. Newman, FORTRAN programs for simulation of electrochemical systems: Dualfoil, University of California, Berkeley, 1998, http://www.cchem.berkeley.edu/jsngrp/fortran.html.

[26] C.M. Doyle, Design and simulation of lithium rechargeable batteries, (Ph.D. thesis), University of California, Berkeley, 1995.

[27] M. Torchio, L. Magni, R.B. Gopaluni, R.D. Braatz, D.M. Raimondo, LIONSIMBA: A Matlab framework based on a finite volume model suitable for Li-ion battery design, simulation, and control, J. Electrochem. Soc. 163 (7) (2016) A1192–A1205.

[28] M.D. Berliner, D.A. Cogswell, M.Z. Bazant, R.D. Braatz, Methods—PETLION: Open-source software for millisecond-scale porous electrode theory-based lithium-ion battery simulations, J. Electrochem. Soc. 168 (9) (2021) 090504.

[29] X. Hu, S. Li, H. Peng, A comparative study of equivalent circuit models for Li-ion batteries, J. Power Sources 198 (2012) 359–367.

[30] C. Speltino, D. Di Domenico, G. Fiengo, A. Stefanopoulou, Comparison of reduced order lithium-ion battery models for control applications, in: Proceedings of the 48h IEEE Conference on Decision and Control Held Jointly with 28th Chinese Control Conference, 2009, pp. 3276–3281.

[31] C. Zou, C. Manzie, S. Anwar, Control-oriented modeling of a lithium-ion battery for fast charging, IFAC Proc. Vol. 47 (3) (2014) 3912–3917.

[32] U. Krewer, F. Röder, E. Harinath, R.D. Braatz, B. Bedürftig, R. Findeisen, Dynamic models of Li-ion batteries for diagnosis and operation: A review and perspective, J. Electrochem. Soc. 165 (16) (2018) A3656–A3673.

[33] B. Suthar, P.W. Northrop, R.D. Braatz, V.R. Subramanian, Optimal charging profiles with minimal intercalation-induced stresses for lithium-ion batteries using reformulated pseudo 2-dimensional models, J. Electrochem. Soc. 161 (11) (2014) F3144–F3155.

[34] R.B. Smith, M.Z. Bazant, Multiphase porous electrode theory, J. Electrochem. Soc. 164 (11) (2017) E3291–E3310.

[35] T.R. Ferguson, M.Z. Bazant, Nonequilibrium thermodynamics of porous electrodes, J. Electrochem. Soc. 159 (12) (2012) A1967–A1985.

[36] T.R. Ferguson, M.Z. Bazant, Phase transformation dynamics in porous battery electrodes, Electrochim. Acta 146 (2014) 89–97.

[37] M.D. Berliner, B. Jiang, D.A. Cogswell, M.Z. Bazant, R.D. Braatz, Fast charging of lithium-ion batteries by mathematical reformulation as mixed continuous-discrete simulation, in: American Control Conference, 2022, pp. 5265–5270.

[38] M.D. Berliner, B. Jiang, D.A. Cogswell, M.Z. Bazant, R.D. Braatz, Novel operating modes for the charging of lithium-ion batteries, J. Electrochem. Soc. 169 (10) (2022) 100546.

[39] A123 Systems official website, http://www.a123systems.com/.

[40] W. Mai, A.M. Colclasure, K. Smith, Model-instructed design of novel charging protocols for the extreme fast charging of lithium-ion batteries without lithium plating, J. Electrochem. Soc. 167 (8) (2020) 080517.

[41] Z. Chen, D.L. Danilov, R.-A. Eichel, P.H.L. Notten, Porous electrode modeling and its applications to Li-ion batteries, Adv. Energy Mater. 12 (32) (2022) 2201506.

[42] J. Newman, W. Tiedemann, Porous-electrode theory with battery applications, AIChE J. 21 (1) (1975) 25–41.

[43] W. Fang, O.J. Kwon, C.-Y. Wang, Electrochemical–thermal modeling of automotive Li-ion batteries and experimental validation using a three-electrode cell, Int. J. Energy Res. 34 (2) (2010) 107–115.

[44] K. Baek, E. Hong, S. Cha, Capacity fade modeling of a lithium-ion battery for electric vehicles, Int. J. Automot. Technol. 16 (2) (2015) 309–315.

[45] W. Gu, C. Wang, Thermal-electrochemical modeling of battery systems, J. Electrochem. Soc. 147 (8) (2000) 2910–2922.

[46] L. Cai, R.E. White, Mathematical modeling of a lithium-ion battery with thermal effects in COMSOL Inc. Multiphysics (MP) software, J. Power Sources 196 (14) (2011) 5985–5989.

[47] S.M. Allen, J.W. Cahn, A microscopic theory for antiphase boundary motion and its application to antiphase domain coarsening, Acta Metall. 27 (6) (1979) 1085–1095.

[48] J.W. Cahn, J.E. Hilliard, Free energy of a nonuniform system. I. Interfacial free energy, J. Chem. Phys. 28 (2) (1958) 258–267.

[49] M.Z. Bazant, Theory of chemical kinetics and charge transfer based on nonequilibrium thermodynamics, Acc. Chem. Res. 46 (5) (2013) 1144–1160.

[50] R.A. Marcus, On the theory of oxidation-reduction reactions involving electron transfer. I, J. Chem. Phys. 24 (5) (1956) 966–978.

[51] R. Marcus, On the theory of oxidation-reduction reactions involving electron transfer. II. Applications to data on the rates of isotopic exchange reactions, J. Chem. Phys. 26 (4) (1957) 867–871.

[52] C.E. Chidsey, Free energy and temperature dependence of electron transfer at the metal-electrolyte interface, Science 251 (4996) (1991) 919–922.

[53] D. Fraggedakis, M. McEldrew, R.B. Smith, Y. Krishnan, Y. Zhang, P. Bai, W.C. Chueh, Y. Shao-Horn, M.Z. Bazant, Theory of coupled ion-electron transfer kinetics, Electrochim. Acta 367 (2021) 137432.

[54] H. Zhao, H. Deng, A. Cohen, J. Lim, Y. Li, D. Fraggedakis, B. Jiang, B. Storey, W. Chueh, R.D. Braatz, M.Z. Bazant, Learning heterogeneous reaction kinetics from X-ray movies pixel-by-pixel, 2022, http://dx.doi.org/10.21203/rs.3.rs-2320040/v1, Research Square preprint.

[55] D. Fraggedakis, N. Nadkarni, T. Gao, T. Zhou, Y. Zhang, Y. Han, R.M. Stephens, Y. Shao-Horn, M.Z. Bazant, A scaling law to determine phase morphologies during ion intercalation, Energy Environ. Sci. 13 (7) (2020) 2142–2152.
[56] T. Gao, Y. Han, D. Fraggedakis, S. Das, T. Zhou, C.-N. Yeh, S. Xu, W.C. Chueh, J. Li, M.Z. Bazant, Interplay of lithium intercalation and plating on a single graphite particle, Joule 5 (2) (2021) 393–414.
[57] D.A. Cogswell, M.Z. Bazant, Size-dependent phase morphologies in $LiFePO_4$ battery particles, Electrochem. Commun. 95 (2018) 33–37.
[58] Y. Guo, R.B. Smith, Z. Yu, D.K. Efetov, J. Wang, P. Kim, M.Z. Bazant, L.E. Brus, Li intercalation into graphite: direct optical imaging and Cahn–Hilliard reaction dynamics, J. Phys. Chem. Lett. 7 (11) (2016) 2151–2156.
[59] Y. Li, F. El Gabaly, T.R. Ferguson, R.B. Smith, N.C. Bartelt, J.D. Sugar, K.R. Fenton, D.A. Cogswell, A. Kilcoyne, T. Tyliszczak, M.Z. Bazant, W.C. Chueh, Current-induced transition from particle-by-particle to concurrent intercalation in phase-separating battery electrodes, Nature Mater. 13 (12) (2014) 1149–1156.
[60] K.E. Thomas-Alyea, C. Jung, R.B. Smith, M.Z. Bazant, In situ observation and mathematical modeling of lithium distribution within graphite, J. Electrochem. Soc. 164 (11) (2017) E3063.
[61] B. Ma, S. Agrawal, R. Gopal, P. Bai, Operando microscopy diagnosis of the onset of lithium plating in transparent lithium-ion full cells, ACS Appl. Mater. Interfaces (2022).
[62] A. Pei, G. Zheng, F. Shi, Y. Li, Y. Cui, Nanoscale nucleation and growth of electrodeposited lithium metal, Nano Lett. 17 (2) (2017) 1132–1139.
[63] D. Baker, M. Verbrugge, Modeling overcharge at lithiated-graphite porous electrodes plating and dissolution of lithium, J. Electrochem. Soc. 167 (10) (2020) 100508.
[64] J. Newman, K.E. Thomas-Alyea, Electrochemical Systems, John Wiley & Sons, Hoboken, New Jersey, 2012.
[65] P. Ramadass, B. Haran, R. White, B.N. Popov, Mathematical modeling of the capacity fade of Li-ion cells, J. Power Sources 123 (2) (2003) 230–240.
[66] A.C. Hindmarsh, P.N. Brown, K.E. Grant, S.L. Lee, R. Serban, D.E. Shumaker, C.S. Woodward, SUNDIALS: Suite of nonlinear and differential/algebraic equation solvers, ACM Trans. Math. Software 31 (3) (2005) 363–396.
[67] J.A.E. Andersson, J. Gillis, G. Horn, J.B. Rawlings, M. Diehl, CasADi – A software framework for nonlinear optimization and optimal control, Math. Program. Comput. 11 (1) (2019) 1–36.
[68] D.D. Nikolić, DAE tools: Equation-based object-oriented modelling, simulation and optimisation software, PeerJ Comput. Sci. 2 (2016) e54.
[69] P.J. Mosterman, An overview of hybrid simulation phenomena and their support by simulation packages, in: International Workshop on Hybrid Systems: Computation and Control, 1999, pp. 165–177.
[70] B. Srinivasan, S. Palanki, D. Bonvin, Dynamic optimization of batch processes: I. Characterization of the nominal solution, Comput. Chem. Eng. 27 (1) (2003) 1–26.
[71] A.E. Bryson, Y.-C. Ho, Applied Optimal Control: Optimization, Estimation, and Control, Routledge, Thames, Oxfordshire, England, UK, 2018.
[72] D.G. Luenberger, Y. Ye, Linear and Nonlinear Programming, Springer, New York, 1984.
[73] M. Schlegel, K. Stockmann, T. Binder, W. Marquardt, Dynamic optimization using adaptive control vector parameterization, Comput. Chem. Eng. 29 (8) (2005) 1731–1751.
[74] K.A. Severson, P.M. Attia, N. Jin, N. Perkins, B. Jiang, Z. Yang, M.H. Chen, M. Aykol, P.K. Herring, D. Fraggedakis, M.Z. Bazant, S.J. Harris, W.C. Chueh, R.D. Braatz, Data-driven prediction of battery cycle life before capacity degradation, Nature Energy 4 (5) (2019) 383–391.
[75] P. Bai, D.A. Cogswell, M.Z. Bazant, Suppression of phase separation in $LiFePO_4$ nanoparticles during battery discharge, Nano Lett. 11 (11) (2011) 4890–4896.
[76] L.O. Valøen, J.N. Reimers, Transport properties of $LiPF_6$-based Li-ion battery electrolytes, J. Electrochem. Soc. 152 (5) (2005) A882–A891.
[77] D.M. Bernardi, J.-Y. Go, Analysis of pulse and relaxation behavior in lithium-ion batteries, J. Power Sources 196 (1) (2011) 412–427.
[78] J.B. Rawlings, D.Q. Mayne, M. Diehl, Model Predictive Control: Theory, Computation, and Design, second ed., Nob Hill Publishing, Madison, WI, 2017.
[79] B. Srinivasan, D. Bonvin, E. Visser, S. Palanki, Dynamic optimization of batch processes: II. Role of measurements in handling uncertainty, Comput. Chem. Eng. 27 (1) (2003) 27–44.
[80] M.D. Berliner, D.A. Cogswell, M.Z. Bazant, R.D. Braatz, A mixed continuous-discrete approach to fast charging of Li-ion batteries while maximizing lifetime, IFAC-PapersOnLine 55 (30) (2022) 305–310.